

Revealing the Competition between Defect-Trapped Exciton and Band-Edge Exciton Photoluminescence in Monolayer Hexagonal WS₂

Ke Wu, Hongxia Zhong, Quanbing Guo, Jibo Tang, Zhenyu Yang, Lihua Qian, Shengjun Yuan,* Shunping Zhang,* and Hongxing Xu

Monolayer transition-metal dichalcogenides grown by chemical vapor deposition (CVD) always contain certain types of defects that dramatically affect their electronic and optical properties. For CVD-grown hexagonal WS₂ monolayer, complex photoluminescence (PL) patterns are commonly observed, but the defect-related optical mechanisms are still not well understood. Here, by combining the optical and structural characterizations and *ab initio* calculations, the correlation between the patterned PL emission and the details of defects in CVD-grown hexagonal WS₂ monolayer are revealed. The temperature-dependent PL spectra show the correlation between the defect-trapped and band-edge exciton emission. The high-resolution scanning transmission electron microscopy identifies the positive correlation between the density of WS₂-vacancy and PL intensity. In the end, the *ab initio* calculations and molecule adsorption PL spectra show that the coexistence of p- and n-doping effects, caused by the W and S complex vacancy, weakens the modulation of molecular adsorption on PL intensity. This work gives new insights into the origin of the inhomogeneous PL distribution in WS₂ monolayer, which provides important guidance in the regulation of electronic and optical properties of transition-metal dichalcogenides via defect engineering.

1. Introduction

Monolayer transition-metal dichalcogenides (TMDs) have attracted tremendous interests due to their unique electronic or optical properties, i.e., direct bandgaps,^[1] strong excitonic effects,^[2,3] strong non-linear effects,^[4–6] and valley-pseudospin,^[7–9] which has great potential for developing new optoelectronic and valleytronic devices. In TMDs, the most common defects like vacancy^[10] and grain boundary^[11] always act as chemical/physical adsorption sites^[12–14] or scattering centers.^[15] They can also create local potential traps for excitons,^[13,16,17] modulate the PL intensity,^[18] change the valley polarization,^[19] or carrier mobility of the materials.^[20] For MoX₂ (X = S/Se), chalcogen vacancies are usually recognized as the radiative or nonradiative recombination sites that would enhance^[14] or suppress^[13] the exciton emission at room temperature. In contrast, for WX₂ (X = S/Se), reports show that tungsten

vacancies^[21–24] may play an important role in creating long-lived valley polarization^[25] or single-photon emission.^[21]

To promote the integration and application of monolayer TMDs, chemical vapor deposition (CVD) has become the preferred method in the preparation of wafer-scale TMDs materials for its high controllability and low cost. However, compared with the exfoliated sample, defects are more prominent in the CVD-grown TMDs.^[24] Usually, there are alternating bright (α) and dark (β) photoluminescence (PL) domains within grown hexagonal WS₂ monolayer.^[22,26,27] The origin of this phenomenon has attracted quite some discussion. Clearly, it is not because of the change of thickness or some strain effects.^[26] A larger trion-to-exciton ratio and a higher oxidative reactivity in the bright domain suggest that there exists some structural difference between the two domains.^[26,27] But for the type of defects, Jeong et al.^[22] found a higher density of S-vacancy in the bright domain but more W-vacancy in the dark domain. Lin et al.^[27] showed that the bright (dark) domain contains more Cr (Fe) substitutional W-vacancy. It is generally accepted that the type and density of defects are responsible for the radiative and nonradiative recombination in hexagonal WS₂ monolayer, which explains the inhomogeneous PL distribution with threefold symmetry. However, the


K. Wu, H. Zhong, Q. Guo, S. Yuan, S. Zhang, H. Xu
School of Physics and Technology and Key Laboratory of Artificial Micro- and Nano-structures of Ministry of Education
Wuhan University
Wuhan 430072, China
E-mail: s.yuan@whu.edu.cn; spzhang@whu.edu.cn

K. Wu, L. Qian
School of Physics
Huazhong University of Science and Technology
Wuhan 430074, China

J. Tang
The Institute for Advanced Studies
Wuhan University
Wuhan 430072, China

Z. Yang
College of Microtechnology and Nanotechnology
Qingdao University
Qingdao 266071, China

H. Xu
School of Microelectronics
Wuhan University
Wuhan 430072, China

 The ORCID identification number(s) for the author(s) of this article can be found under <https://doi.org/10.1002/adom.202101971>.

DOI: 10.1002/adom.202101971

actual correlation between the defects, band-edge exciton, and defect-trapped exciton emission is still not completely understood.

In this paper, we explore the type, density, and role of the defects in generating the alternating PL domains of hexagonal WS₂ monolayer. The defects provide trapped states that can deplete the band-edge excitons emission at low temperature. From scanning transition electron microscopy (STEM) characterization, we find that the W and S complex vacancy (WS_x-vacancy) defects density is positively correlated to the PL intensity. The bright region with higher WS_x-vacancy density exhibits higher defect-trapped exciton PL intensity than that of the dark region with lower WS_x-vacancy density. Combining with ab initio calculations, we deduce that WS-vacancy with the lowest formation energy in WS_x-vacancy ($x = 1-6$) would be the most likely defect. WS-vacancy brings both donor and acceptor levels in the bandgap, suppressing the PL fluctuation caused by the doping effects in molecule adsorption experiments. Our experiments provide insight into the relationship between exciton emission and defect structure of TMDs.

2. Experimental Results

We synthesize monolayer WS₂ by the CVD method (see the Experimental Section and Figure S1, Supporting Information). Figure 1a shows an optical image of the monolayer hexagonal WS₂ on the Si substrate with 285 nm SiO₂. The corresponding PL image is taken in atmospheric condition using a halogen lamp and a 532 nm filter set which contains a 590 nm long-pass filter (Figure 1b). Interestingly, the PL image presents alternating bright (α) and dark (β) PL domains with threefold symmetry. The layer thickness and crystal orientation are not the reasons for this kind of PL domain, more details can be found in the second-harmonic generation (SHG), atomic force microscope (AFM), and energy-dispersive spectrometer (EDS) characterization results (Figures S2 and S3, Supporting Information). To explore the mechanism of the alternating PL intensity, we choose six typical positions along the perpendicular of the hexagonal. The corresponding room-temperature PL spectra of the six positions are shown in Figure 1c. The spectra exhibit only one peak around 1.97 eV which can be deconvoluted into the neutral exciton (A⁰) and charged exciton (A'). For simplicity,

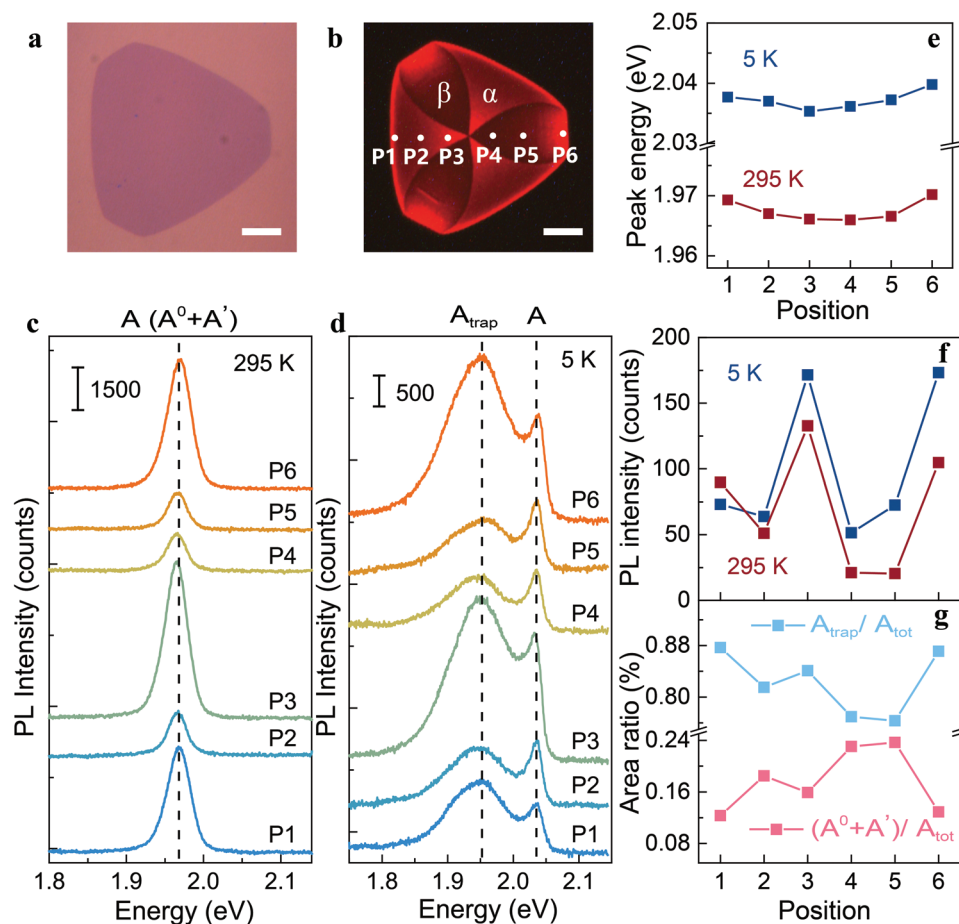


Figure 1. a,b) Optical image and PL image of hexagonal monolayer WS₂ on SiO₂/Si substrate, respectively. Scale bar: 15 μ m. The bright and dark PL domains are denoted as α and β , respectively. The test positions are marked by Arabic numerals from 1 to 6. c,d) The PL spectra of the six test positions measured at 295 and 5 K, respectively. e) The A⁰ excitonic peak as a function of test position. We use Lorentz and Gaussian convolution to fit the PL spectra. f) Comparing the total PL intensity of the six test positions measured at 295 and 5 K. g) Comparing the defect-trapped and A excitons emission ratio in the total PL emission at 5 K.

A exciton includes both A^0 and A' exciton in all the discussions in this work. When the sample is cooled down to 5 K, the A exciton blueshifts to 2.03 eV. A new broad peak shows up around 1.95 eV, which is recognized as the defect-trapped exciton (A_{trap}) emission in TMDs (Figure 1d).^[10,17,28] The much broader peak width of A_{trap} is related to the stronger interactions between the defect-trapped exciton and phonons.^[29] For the six positions, the energy of A^0 exciton varies in the range of 5 meV between 295 and 5 K (Figure 1e). At the edge of the domains, the PL exhibits a stronger intensity and a blueshift corresponding to the inner region. Then we plot the total PL intensity of the six positions measured at 295 and 5 K (Figure 1f). Clearly, the spatial variation of the PL intensity is independent of temperature. The defect-trapped exciton emission also shows a similar variation behavior with that of the total PL intensity, but the A exciton emission follows an opposite one (Figure 1g). These results show that the defect-trapped exciton emission dominates the alternating bright and dark PL distribution at 5 K, whereas the A exciton emission dominates the PL distribution at 295 K.

Figure 2a,b shows the temperature-dependent PL spectra of two typical points in the α domain (P3) and β domain (P4), respectively. We plot the PL intensity of the defect-trapped

excitons (A_{trap}), A excitons, and the total emission (A_{tot}) as a function of the temperature in Figure 2c. It can be easily noted that the difference of the PL intensity between P3 and P4 is dominated by A_{trap} emission at low temperature, which quickly quenches with the increasing temperature. When the temperature is higher than 60 K, A exciton emission starts to dominate the PL spectra. This temperature intersection of A exciton and A_{trap} emission intensity of monolayer WS_2 (60 K) is much lower than that of monolayer MoS_2 (250 K).^[15] In addition, we notice that the A_{tot} undergoes a process of decreasing first and then increasing with the increasing temperature. These phenomena suggest that A exciton emission competes with A_{trap} emission with the increasing temperature. However, the optically dark state, which lies below the bright state in monolayer WS_2 , makes the competition between A and A_{trap} more complicated than MoX_2 ($X = \text{S/Se}$) materials.^[15,30] Based on the three-state model in previous reports,^[15] here we use a four-state model to explain the PL variation of WS_2 with the increasing temperature, as shown in Figure 2d. Due to the spin-orbit splitting, the conduction band of monolayer WS_2 splits into two conduction bands with inverse spin-polarization. The spin polarization of electrons in the upper (lower) conduction band matches (opposite) with those in the upper valence band. Here, the red and

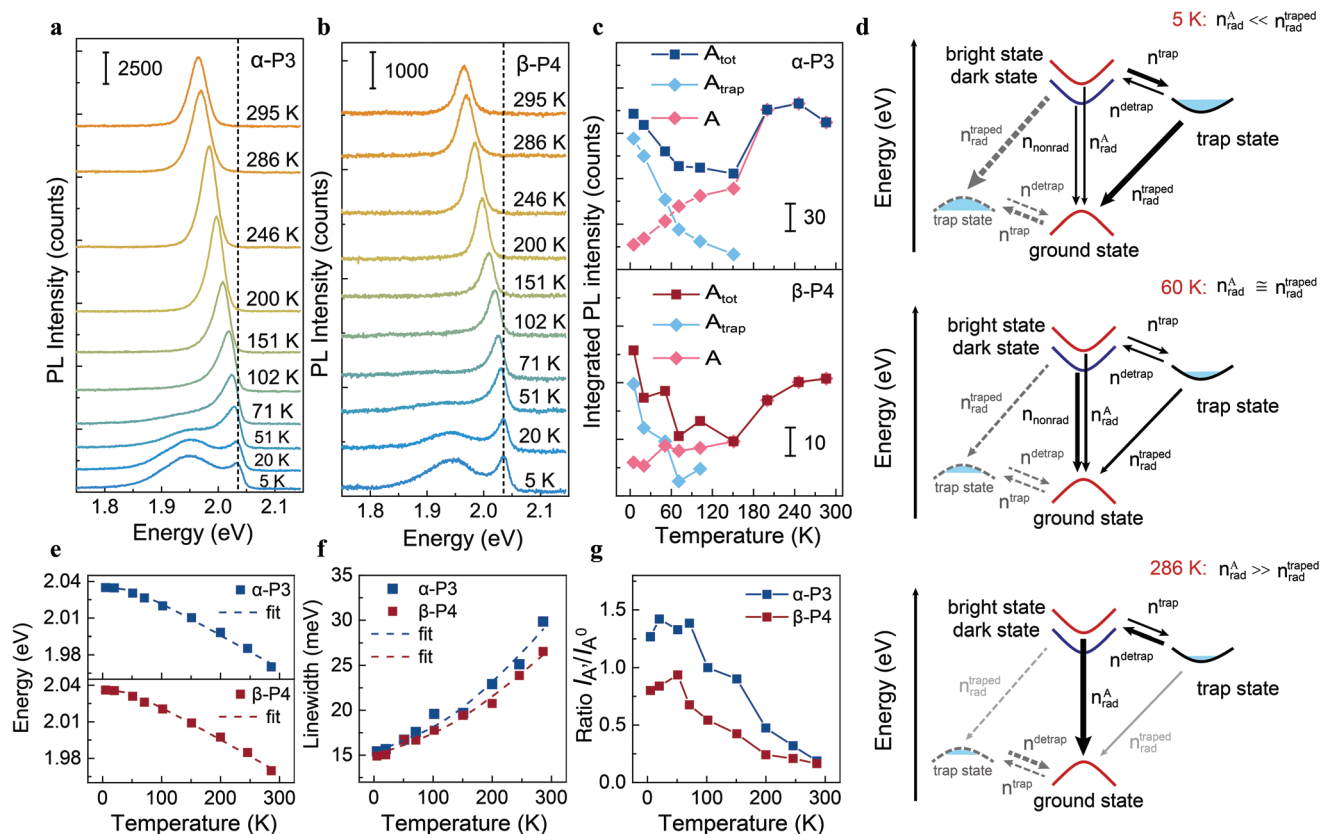


Figure 2. a,b) The temperature-dependent PL spectra of the α -P3 and β -P4, respectively. The vertical dotted lines indicate the A excitonic peak at 5 K. c) The PL intensity of the A, A_{trap} , and A_{tot} at α -P3 (up) and β -P4 (down) as a function of temperature. In the process of temperature rising from 286 to 295 K, the pressure of the cryostat will increase by an order of magnitude due to the performance of the equipment. This will reduce the PL intensity at 295 K greatly. Therefore, we only fit the temperature-dependent PL spectra from 5 to 286 K. d) A four-state model, including the bright, dark, defect-trap, and ground state, explains the competition between the A and A_{trap} emission at different temperature. The defect-trap state is introduced by the n- (black solid line) or p- (gray dotted line) doping defect. But the contribution of these two kinds of defect-trap states to the A_{trap} emission cannot be distinguished here. e–g) The peak energy, the linewidth of A^0 exciton, and the ratio $I_{A'}/I_{A^0}$, respectively, are plotted as a function of temperature, respectively.

blue conduction bands correspond to the bright (upper) and dark (lower) excitonic state, respectively. The red valence band corresponds to the ground state. The trap-state introduced by the n- (right black solid line) or p- (left gray dotted line) doping defect are also included. We first consider the trap-state introduced by the n-doping defect. At 5 K, most of the electrons at excited states (n^{trap}) are captured into the trap-state and decay radiatively, only a small number of electrons (n^{detrap}) can use the insufficient thermal energy to reach the bright state (A exciton). This results in the high A_{trap} and low A exciton emission ($n_{\text{rad}}^{\text{A}}$) at 5 K, as shown in Figure 2a,b. Considering the comparable A_{tot} value at 5 and 286 K, we infer that only a small part of electrons on the bright state would relax to the dark state and undergo a nonradiative transition ($n_{\text{nonrad}}^{\text{D}}$) at 5 K due to the participation of the trap-state. Figure 2d (II) depicts the competing transition at 60 K. With the increasing temperature, even though the A exciton emission increases, both the A_{trap} and A_{tot} decrease quickly. It suggests that although some electrons can escape from the trap-state using the available thermal energy, detrapped electrons or a portion of band-edge electrons would relax to the dark state and undergo the nonradiative transition ($n_{\text{nonrad}}^{\text{D}}$). When the temperature continues to rise to 286 K, the excited electrons can use sufficient thermal energy to avoid relaxing to the dark state or being trapped at the defect state and staying at the bright state (Figure 2d III). This leads to the high A exciton intensity and missing A_{trap} emission at 286 K. For the trapping to those defects lie below the Fermi level (gray dotted line in Figure 2d), we can understand the whole process in a similar way, as described in Section 1.1 of the Supporting Information. The relative contribution of these two kinds of defect-trapped exciton emission to the total emission A_{trap} will be discussed in the following experiments and calculations.

We further extract the relationship between the energy and peak width of A^0 with temperature from the temperature-dependent PL spectra.^[31,32] The energy shifts of A^0 exciton of the six test positions can be well fitted using both O'Donnell's^[33] or Varshni's^[34] formulae which describe the bandgap dependence on temperature. All the R-squares of the fittings can reach 0.993. Figure 2e shows the fitting example using O'Donnell's formulae

$$E_g(T) = E_0 - S\langle\hbar\omega\rangle\left[\coth\left(\frac{\langle\hbar\omega\rangle}{2k_B T}\right) - 1\right] \quad (1)$$

where E_0 is the optical bandgap at absolute zero, $\langle\hbar\omega\rangle$ is the average phonon energy, S is a coupling strength, and k_B is the Boltzmann's constant. The fitting parameters are given in Table 1. $\langle\hbar\omega\rangle$ is ≈ 12 meV for the six positions, and were fixed in the fitting process. The S parameter, related to the degree of lattice vibration, shows no obvious dependence on the PL intensity of the test positions.

The evolution of the linewidth with the temperature of the A^0 exciton in the sample can be reproduced by a typical form

$$\gamma(T) = \gamma_0 + \sigma T + \gamma' \frac{1}{e^{\hbar\omega/kT} - 1} \quad (2)$$

used to describe the width broadening of the ground state exciton in semiconductors^[31,32] (Figure 2f). Parameter γ_0 is the width broadening at 0 K. The second and last terms describe the width broadening caused by the interaction of exciton with acoustic phonons (σ) and longitudinal optical (LO) phonons (γ'), respectively. The LO-phonon energy $\hbar\omega$ is fixed at 43.89 meV (354 cm^{-1}) in the fitting process. The fitting results are shown in Table 1. We find that γ_0 only increases a little at the edge P1 and P6. This variation can be related to the lattice structural difference at the sample edge, which will be characterized later. The influence caused by the second term can be ignored due to the small σ which is about 0.02 meV K^{-1} for all the positions. In contrast, γ' exhibits a positive correlation with the ratio of $I_{\text{trap}}/I_{\text{tot}}$. γ' of P1, P3, and P6 is much larger than that of P2, P4, and P5 which have smaller $I_{\text{trap}}/I_{\text{tot}}$ at low temperature (Table 1). Considering the competitive process between A_{trap} and A exciton emission with the increasing temperature, this phenomenon can be understood as follows. For the region with larger $I_{\text{trap}}/I_{\text{tot}}$, the probability of scattering the n_{trap} electrons (holes) from the trap-state to the excitonic state (top valence band) through the annihilation of LO-phonon is much higher than that at the region with smaller $I_{\text{trap}}/I_{\text{tot}}$ when the temperature rises. And this leads to a faster broadening rate (larger γ') of exciton linewidth with the increasing temperature at region (P1, P3, P6) with larger $I_{\text{trap}}/I_{\text{tot}}$ and vice versa. In addition, the region with larger $I_{\text{trap}}/I_{\text{tot}}$ owns a higher PL ratio I_A/I_{A^0} and the similar phenomenon can be found in previous reports.^[26,27] Figure 2g shows the ratio I_A/I_{A^0} of P3 and P4. The difference in the ratio I_A/I_{A^0} between P3 and P4 gradually decreases as the temperature increases. Both the faster linewidth broadening

Table 1. The fitting parameters were obtained from the temperature-dependent energy and line-shape broadening of A^0 exciton at P1–P6 in hexagonal monolayer WS₂.

Parameter	α -P1	α -P2	α -P3	β -P4	β -P5	β -P6
$A_{\text{trap}}/A_{\text{tot}}$ (5 K)	0.87	0.81	0.84	0.77	0.76	0.87
W-vacancy [%]	–	0.09	0.17	0.09	0.09	–
Using Equation (1)						
E_0 [eV]	2.036	2.036	2.034	2.035	2.036	2.039
$\langle\hbar\omega\rangle$ [meV]	12	12	12	12	12	12
S	1.6	1.63	1.61	1.62	1.63	1.61
Using Equation (2)						
γ_0 [meV]	16	15	15	15	15	16
γ' [meV]	33	18	31	22	18	40

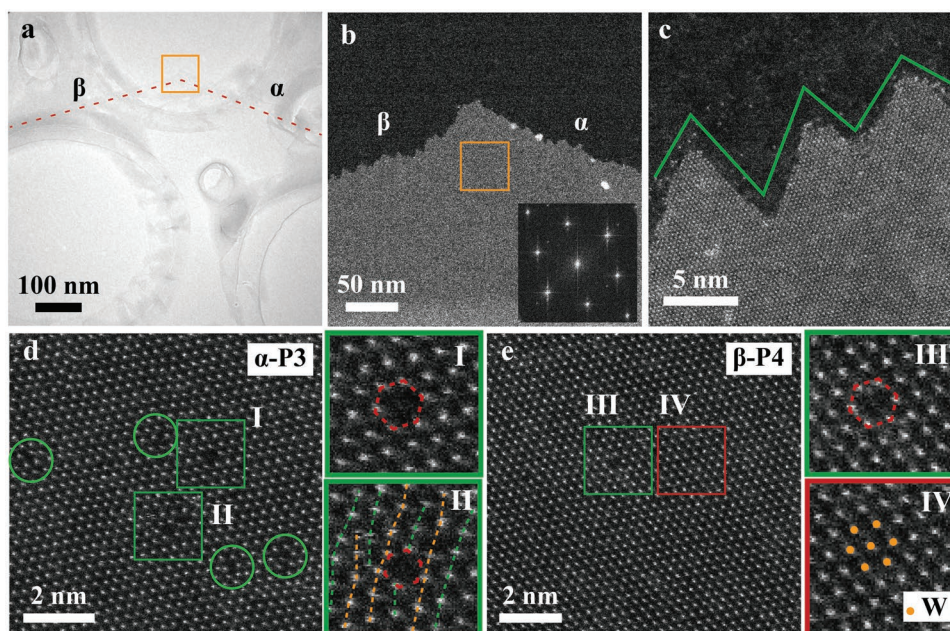


Figure 3. a) A low-magnification STEM image of the hexagonal monolayer WS₂. The red dotted line indicates the sample edge of the α and β domains. b) The magnified STEM image of the orange square in (a). The corresponding Fourier transform image is shown at the lower right corner. c) The magnified STEM image of the sample edge. The green lines are used to sketch the boundary morphology. d,e) The atomic-resolution STEM images of α -P3 and β -P4 domains, respectively. The magnified STEM images in red and green squares are shown on the right side of the corresponding image. The green circles indicate the dislocation of the tungsten. The colorful dotted line in the inset image II in (d) depicts the chain of the W atom. In the inset image IV in (e), the orange dots superimposed on the W atom highlight the regular arrangement of the W atom.

and higher trion emission indicate that P3 may have higher defect density or varied type compared to that of P4.

To explore the origin of the temperature-dependent A and A_{trap} emission, we characterize the lattice structures of the bright (α) and dark (β) PL domains in the hexagonal WS₂ using high-resolution scanning transmission electron microscopy (STEM), as shown in **Figure 3**. Figure 3a is a low-magnification STEM image of the corner of hexagonal WS₂. The red dotted

line is drawn along the edge of the α and β domains. And the magnified STEM image of the orange rectangle area is shown in Figure 3b. The single crystal property of α and β domain can be confirmed from the Fourier transform image of the orange rectangle inside (inset in Figure 3b). Figure 3c shows the STEM image of the sample edge, which is serrated (marked by the green line). Compared to the inner part, the enhanced PL intensity and blueshifted PL peak (Figure 1) at this serrated edge, indicate that there may exist some dangling bonds which would result in higher doping effects. The subtle enhanced PL at the sample edge in the atmosphere also supports this inference (**Figure 4**). Figure 3d (3e) shows the STEM image of P3 (P4). No variation of defect type is observed at bright and dark PL areas, except a small variation in WS_x-vacancy density (Table 1). Here, the number (x) of S atom vacancies around the W vacancy is undistinguishable due to its small nucleus. In principle, the value of x should be a number from 0 to 6 and will be figured out via the following combination of experimental and theoretical approaches. In the first-principles calculations, we consider several types of defects with different values of x as shown in Figure S6 (Supporting Information). The red rectangle in Figure 3e reveals the perfect WS₂ lattice and orange dots in IV are superimposed on the W atom to highlight the arrangement. The green rectangle (image I–III) inset points out the WS_x-vacancy site and the magnified STEM image is on the right side of the corresponding image. Except for the WS_x-vacancy, dislocations of W atoms are also circled out by green circles. A typical dislocation around WS_x-vacancy is depicted by orange and green dotted lines in Figure 3g II. According to the statistics, the density of WS_x-vacancy (based on the defect density of W vacancies) in P3 is about 0.17%

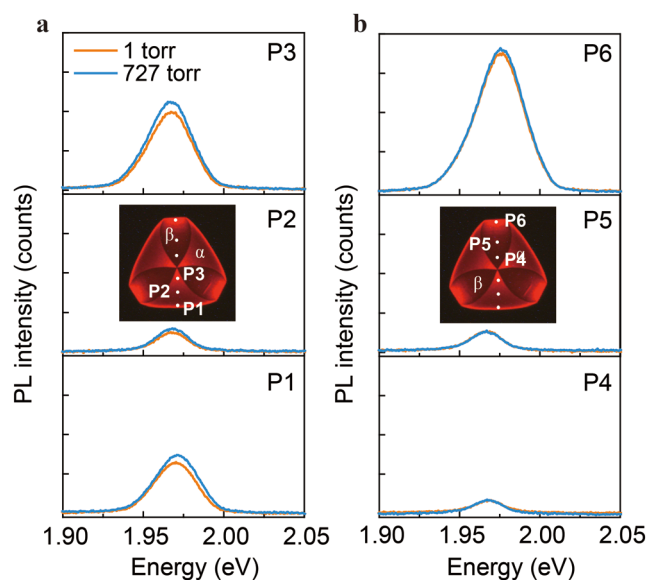


Figure 4. PL spectra of the WS₂ sample measured under different pressure, 1 Torr (orange) and 727 Torr (blue).

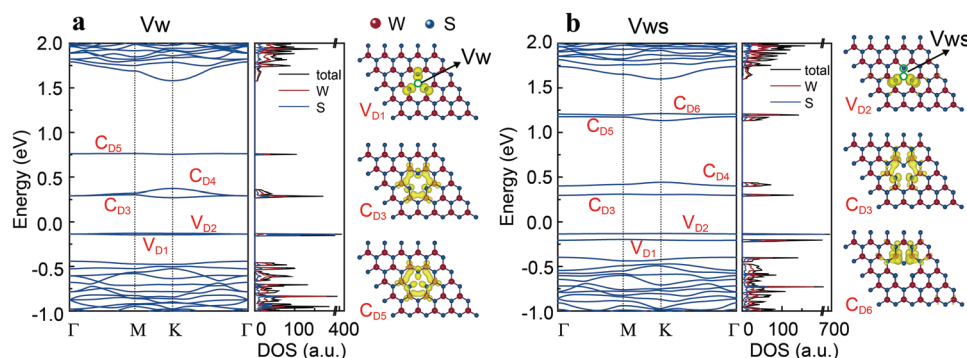


Figure 5. The band structure, partial density of states (DOS), and isosurfaces of the labeled defect states for single a) V_w defects and b) V_{ws} defects. The Fermi level is set to zero. The red (blue) ball represents the W (S) atom. The vacancy sites are circled by a green solid line. In the band structure, the defect (D) states are labeled as V_D (C_D) for occupied (unoccupied) states. The isosurface value is $0.002 \text{ e} \text{ \AA}^{-3}$.

($1.9 \times 10^{12} \text{ cm}^{-2}$) which is a little higher than 0.09% ($9.9 \times 10^{11} \text{ cm}^{-2}$) at P4 area (Table 1). The higher WS_x -vacancy density can always be found in the WS_2 monolayer with higher A_{trap} emission. The A_{trap} (A_{tot}) of the bright area with 0.54% WS_x -vacancy is 9 (4.8) times larger than that of the dark area, with 0.06% vacancy, as shown in Figure S5. These results reveal a qualitative relationship that the A_{tot} and A_{trap} intensity are proportional to the WS_x -vacancy density. Based on the PL and STEM characterizations, we conclude that both the faster peak width-broadening of the excitons and larger ratio A'/A^0 at the bright domain (P1, P3, P6) can be attributed to the scattering effect and higher doping effect caused by the higher WS_x -vacancy density, dislocation (P3), or the dangling bonds at the serrated edge (P1, P6).

In the following, we deduce the x value in WS_x -vacancy through the molecule adsorption PL characterization, calculation of defects formation energy, and doping effects. According to the previous reports, for MoX_2 ($X = S/Se$) material, the physisorption of O_2/H_2O molecules at the defects would enhance the PL emission significantly.^[14] In contrast, the physisorption of O_2/H_2O would quench the PL intensity of WSe_2 . The differences between MoX_2 and WX_2 materials at physisorption of O_2/H_2O are attributed to the p-doping effect of the O_2/H_2O molecule physical adsorption on different semiconductor types, which usually depend on the type of intrinsic defect or externally introduced dopants.^[14] For MX_2 materials, the most common intrinsic chalcogen vacancies always bring acceptor levels near conduction band minimum (CBM) and the metal vacancies would bring donor levels near valence band maximum (VBM), resulting in the common n-type (MoX_2) or p-type (WX_2) semiconductor properties, respectively. However, for WS_2 , the situation is different. In our experiment, the O_2/H_2O physical adsorption has little effect on the PL intensity of WS_2 , except small PL increment at the region with high W-vacancy density or the sample edge as shown in Figure 4.

In the experiment of adsorption and desorption of air molecules, the WS_2 sample is put into the vacuum chamber and the pristine PL spectra of P1–P6 were measured at the atmospheric environment (727 Torr) using a 532 nm continuous-wave laser. Then, the chamber is evacuated to 1 Torr to remove the physically adsorbed O_2 and H_2O molecules in the air and the PL spectra at the same sites are measured again. Figure 4 shows the PL spectra measured under different pressure. The

variations of PL intensity at P2, P4, P5, and P6 are almost neglectable. Even though the PL intensity of P1 and P3 at 727 Torr is a little lower than that at 1 Torr, it can be easily noted that the doping effects caused by the physisorption of O_2 or H_2O molecules are not the dominant reason for the segmented PL distribution in the hexagonal WS_2 . What's more, the WS_x -vacancy defect should be a complex defect where the x value should not be zero. Because the W-vacancy (V_w) defects would lead to p-doping, the PL intensity would increase much after the desorption of air molecules. This is not consistent with our results. Pure O_2 molecules experiment shows the same results which are not exhibited here. Then calculation results would help us further confirm the inference above and the x value in WS_x -vacancy.

Figure 5a shows the calculation results about W-vacancy (V_w) defect in monolayer WS_2 . The V_w induces two nearly degenerate occupied defect states in the valence band, labeled as V_{D1} and V_{D2} , and three unoccupied defect states C_{D3} , C_{D4} , and C_{D5} in the gap. The partial density of states and plotted isosurfaces show that the defect states are localized around the defect site and the occupied defect state V_{D1} is dominated by p orbitals of S. By contrast, the unoccupied defect states C_{D3} and C_{D5} consist primarily of d orbitals of W, similar to the band edge of pristine WS_2 . The localized defect states are close to the VBM of pristine WS_2 , leading to the p-type doping in the WS_2 monolayer. This agrees with the general rules of transition-metal vacancy defects in TMDC materials.^[35] Then we calculate the formation energy (Table S1 and Figure S6, Supporting Information) and the electronic structure of complex WS_x -vacancy (V_{ws_x}) ($x = 1-6$) (Figure 5b and Figure S7, Supporting Information) to analyze its formation possibility. It is shown that the W-vacancy can be stabilized by one S-vacancy no matter in S- or W-rich environment and therefore the WS-vacancy (V_{ws}) is the most likely defect in V_{ws_x} . In Figure 5b, the V_{ws} induces six localized defect states, including two occupied defect states V_{D1} and V_{D2} , two lower unoccupied defect states C_{D3} and C_{D4} , and two higher unoccupied defect states C_{D5} and C_{D6} . The occupied defect states are dominated by p orbitals of S, while the unoccupied defect states mainly contain d orbitals of W. Because the created localized defect states are close to the conduction and valence band, the studied V_{ws} complex defects lead to both n-type and p-type doping at the same time, which is very

different from the polar p-type doping by Vw defect. This can be related to the p-type doping by single Vw defects and n-type doping by single Vs defects.

Above all, the WS_x-vacancy which brings both donor and acceptor levels into the bandgap may make WS₂ like a bipolar semiconductor. Therefore, the PL variation degree in physisorption of O₂/H₂O molecules experiment can be related to the asymmetry degree of the acceptor–donor levels. Combined with calculated results and molecular adsorption experiments, we deduce that the experimental observed WS_x-vacancy is more likely to be WS-vacancy with the lowest formation energy rather than single W-vacancy defects. The relatively symmetry donor and acceptor level brought by the defects weaken the doping effect caused by the molecule adsorption. These results indicate that the defect states both above and below the Fermi level contribute simultaneously to the total A_{trap} emission if they do affect the PL.

3. Discussion

We also note that the PL segmentation in hexagonal WS₂ has been ascribed to different types of defects. Jeong suggests that the α domain with higher PL intensity is a sulfur-vacancy rich domain.^[22] The energy of the A-exciton peak in the α domain is lower than that in the β domain which contains W-vacancy. In our case, there is no significant relationship in the energy of A exciton between the α and β domains. We also do not observe an obvious correlation between the doping-related A_{1g} mode and the PL intensity, i.e., the blueshift of A_{1g} mode in the β domain compared with the α domain has been found in the report (not shown here). We believe these differences are caused by the different W source and grown methods, which would create different defects in the sample, for example, Jeong et al. use (NH₄)₆H₂W₁₂O₄₀·xH₂O and we use WO₃ powder as W source. On the other hand, our experimental results from the physisorption of O₂/H₂O molecules also do not support the conclusion that the bright α domain mainly contains S-vacancy which may create n-type WS₂ semiconductor. In contrast, Lin et al.^[27] who grow hexagonal WS₂ with WO_{2.9} and S powder report the similar PL spectra properties with us, i.e., the higher trion to exciton ratio in the region with higher PL intensity. Even though they reveal the substitutional metal dopants in the materials, they claim that the impurities replacing W atoms arise from the salt used in their experiments, which is different from our case. In addition, we found that the H₂ can lead to multilayer WS₂ growth and much more impurities compared with the sample grown in pure Ar gas (Figure S4, Supporting Information). A similar phenomenon can be found in Lin's reports. Of course, the above conclusions do not exclude the possibility that no physisorption actually happens during the change of atmosphere of the sample.

4. Conclusion

In this work, we reveal the relationship between the defect-trapped exciton emission, exciton emission, and the complex defect WS-vacancy in the hexagonal monolayer WS₂ with the alternating bright and dark domains. Based on the

temperature-dependent PL characterizations, we use a four-state model to depict the competition between the defect-trapped exciton emission and band-edge exciton emission. The STEM image further reveals a positive correlation between the density of WS_x-vacancy and PL intensity. Then the calculated electronic structure of the defective WS₂ and the molecule adsorption experiments show that the WS-vacancy is the most likely defect due to its lowest formation energy. Relatively symmetry defect level in the bandgap brought by the WS-vacancy will lead to both n- and p- doping effects which would suppress the PL variation caused by the doping effect in the molecule adsorption experiments. Our study on the origin of the alternating PL properties in CVD-grown monolayer WS₂ will accelerate the application process of two-dimensional materials based on defect engineering.

5. Experimental Section

Synthesis of Monolayer WS₂: The monolayer WS₂ samples were grown by chemical vapor deposition on Si substrate with 285 nm SiO₂. The silicon substrate got through ultrasonic cleaning in acetone, ethanol, and deionized water for 20 min, respectively. A quartz boat containing 0.2 g of WO₃ (Alfa Aesar, purity of 99.5%) was put at the center of the furnace, and the eight pieces of substrates were positioned above the WO₃ powder and face-down. And 0.3 g sulfur powder (Alfa Aesar, purity of 99.5%) was placed 20 cm away from the quartz boat. Argon (100 sccm) was used as carrier gas. The WO₃ and sulfur powder were heated separately to 950 and 175 °C and held for 15 min. A schematic diagram of the substrate locations and the time sequence of the heating can be found in Figure S1 (Supporting Information).

Photoluminescence and Raman Spectroscopy: All PL and Raman spectra were excited by a continuous wave 532 nm laser. The PL and Raman signals, acquired at room temperature, were collected by a 100× Olympus objective (NA = 0.9) and dispersed by a blazed grating (PL: 300 lines mm⁻¹, Raman: 1800 lines mm⁻¹). The spectrometer is Renishaw inVia. The temperature-dependent PL spectra were collected by a 50× Olympus objective (NA = 0.5) and dispersed by a 300 lines mm⁻¹ grating, using Montana Instruments Cryostation. The spectrometer is iHR550.

STEM Sample Preparation and Characterizations: The polystyrene (PS)/WS₂ was transferred onto the Cu grids, and PS was dissolved in chloroform. Then the sample was rinsed in deionized water. The WS₂ crystal was examined by JEOL ARM-200F (200 kV) in the School of Materials Science and Engineering, Shanghai Jiao Tong University, China.

Density Functional Theory Calculations: The calculations are performed using the projector augmented wave (PAW) method^[36] implemented in the Vienna ab initio simulation package (VASP) code.^[37] Perdew, Burke, and Ernzerhof (PBE) form of the generalized gradient approximation (GGA) exchange-correlation functional,^[38] and the PAW pseudo potentials^[36] were adopted. A 5 × 5 × 1 supercell was adopted to model the vacancy defects in WS₂. The cut-off energy was set to 500 eV after convergence tests. A Γ -centered Monkhorst-Pack k-point grid^[39] of 4 × 4 × 1 was used for relaxations and the grid of 7 × 7 × 1 for property calculations. In the current calculations, the total energy was converged to less than 10⁻⁶ eV, and the maximum force is less than 0.01 eV Å⁻¹ during the optimization. A vacuum space along the z-axis is larger than 20 Å to avoid spurious interactions. During the structure relaxation, the lattice constants are fixed, and the coordinates of all atoms are fully relaxed.

Supporting Information

Supporting Information is available from the Wiley Online Library or from the author.

Acknowledgements

K.W. and H.Z. contributed equally to this work. This work was supported by the National Natural Science Foundation of China (Grant Nos. 91850207, 12104421, 51771078, 12134011, and 11947218), the National Key R&D Program of China (Grant Nos. 2017YFA0303504 and 2018YFA0305800), the Fundamental Research Funds for the Central Universities, the Strategic Priority Research Program of Chinese Academy of Sciences (Grant No. XDB30000000), China National Postdoctoral Program for Innovative Talents (BX2021195), and China Postdoctoral Science Foundation (2021M692199). Numerical calculations presented in this paper were performed on a supercomputing system in the Supercomputing Center of Wuhan University. The authors acknowledge the assistance from Prof. Qihua Xiong's group (Tsinghua University) for the help of AFM, SEM, and EDS measurements.

Conflict of Interest

The authors declare no conflict of interest.

Data Availability Statement

The data that support the findings of this study are available from the corresponding author upon reasonable request.

Keywords

chemical vapor deposition, complex vacancy, defect-trapped excitons, photoluminescence patterns, WS₂

Received: September 14, 2021

Revised: December 4, 2021

Published online:

- [1] K. F. Mak, C. Lee, J. Hone, J. Shan, T. F. Heinz, *Phys. Rev. Lett.* **2010**, *105*, 136805.
- [2] A. Chernikov, T. C. Berkelbach, H. M. Hill, A. Rigosi, Y. Li, O. B. Aslan, D. R. Reichman, M. S. Hybertsen, T. F. Heinz, *Phys. Rev. Lett.* **2014**, *113*, 076802.
- [3] A. Ramasubramaniam, *Phys. Rev. B* **2012**, *86*, 115409.
- [4] Q. Guo, Z. Ou, J. Tang, J. Zhang, F. Lu, K. Wu, D. Zhang, S. Zhang, H. Xu, *Nano Lett.* **2020**, *20*, 7956.
- [5] L. M. Malard, T. V. Alencar, A. P. M. Barboza, K. F. Mak, A. M. De Paula, *Phys. Rev. B* **2013**, *87*, 201401.
- [6] N. Kumar, S. Najmaei, Q. N. Cui, F. Ceballos, P. M. Ajayan, J. Lou, H. Zhao, *Phys. Rev. B* **2013**, *87*, 161403(R).
- [7] R. Roldán, J. A. Silva-Guillén, M. P. López-Sancho, F. Guinea, E. Cappelluti, P. Ordejón, *Ann. Phys.* **2014**, *526*, 347.
- [8] O. V. Yazyev, A. Kis, *Mater. Today* **2015**, *18*, 20.
- [9] A. Kormányos, G. Burkard, M. Gmitra, J. Fabian, V. Zólyomi, N. D. Drummond, V. Fal'ko, *2D Mater.* **2015**, *2*, 022001.
- [10] P. K. Chow, R. B. Jacobs-Gedrim, J. Gao, T. M. Lu, B. Yu, H. Terrones, N. Koratkar, *ACS Nano* **2015**, *9*, 1520.
- [11] H. Nan, Z. Wang, W. Wang, Z. Liang, Y. Lu, Q. Chen, D. He, P. Tan, F. Miao, X. Wang, J. Wang, Z. Ni, *ACS Nano* **2014**, *8*, 5738.
- [12] S. Mouri, Y. Miyauchi, K. Matsuda, *Nano Lett.* **2013**, *13*, 5944.
- [13] H. V. Han, A. Y. Lu, L. S. Lu, J. K. Huang, H. Li, C. L. Hsu, Y. C. Lin, M. H. Chiu, K. Suenaga, C. W. Chu, H. C. Kuo, W. H. Chang, L. J. Li, Y. Shi, *ACS Nano* **2016**, *10*, 1454.
- [14] S. Tongay, J. Zhou, C. Ataca, J. Liu, J. S. Kang, T. S. Matthews, L. You, J. Li, J. C. Grossman, J. Wu, *Nano Lett.* **2013**, *13*, 2831.
- [15] A. J. Goodman, A. P. Willard, W. A. Tisdale, *Phys. Rev. B* **2017**, *96*, 121404.
- [16] S. Tongay, J. Suh, C. Ataca, W. Fan, A. Luce, J. S. Kang, J. Liu, C. Ko, R. Raghunathanan, J. Zhou, F. Ogletree, J. Li, J. C. Grossman, J. Wu, *Sci. Rep.* **2013**, *3*, 2657.
- [17] M. S. Kim, S. J. Yun, Y. Lee, C. Seo, G. H. Han, K. K. Kim, Y. H. Lee, J. Kim, *ACS Nano* **2016**, *10*, 2399.
- [18] M. Amani, D.-H. Lien, D. Kiriya, J. Xiao, A. Azcatl, J. Noh, S. R. Madhvapathy, R. Addou, K. C. Santosh, M. Dubey, K. Cho, R. M. Wallace, S.-C. Lee, J.-H. He, J. W. Ager, X. Z. Lii, E. Yablonovitch, A. Javey, *Science* **2015**, *350*, 1065.
- [19] K. M. McCreary, M. Currie, A. T. Hanbicki, H. J. Chuang, B. T. Jonker, *ACS Nano* **2017**, *11*, 7988.
- [20] I. S. Kim, V. K. Sangwan, D. Jariwala, J. D. Wood, S. Park, K. S. Chen, F. Y. Shi, F. Ruiz-Zepeda, A. Ponce, M. Jose-Yacamán, V. P. Dravid, T. J. Marks, M. C. Hersam, L. J. Lauhon, *ACS Nano* **2014**, *8*, 10551.
- [21] S. Zhang, C. G. Wang, M. Y. Li, D. Huang, L. J. Li, W. Ji, S. W. Wu, *Phys. Rev. Lett.* **2017**, *119*, 046101.
- [22] H. Y. Jeong, Y. Jin, S. J. Yun, J. Zhao, J. Baik, D. H. Keum, H. S. Lee, Y. H. Lee, *Adv. Mater.* **2017**, *29*, 1605043.
- [23] Z. T. Wu, W. W. Zhao, J. Jiang, T. Zheng, Y. M. You, J. P. Lu, Z. H. Ni, *J. Phys. Chem. C* **2017**, *121*, 12294.
- [24] X. Y. Wang, J. D. Dan, Z. L. Hu, J. F. Leong, Q. Zhang, Z. Y. Qin, S. S. Li, J. P. Lu, S. J. Pennycook, W. X. Sun, C. H. Sow, *Chem. Mater.* **2019**, *31*, 7970.
- [25] W.-T. Hsu, Y.-L. Chen, C.-H. Chen, P.-S. Liu, T.-H. Hou, L.-J. Li, W.-H. Chang, *Nat. Commun.* **2015**, *6*, 8963.
- [26] Y. Sheng, X. Wang, K. Fujisawa, S. Ying, A. L. Elias, Z. Lin, W. Xu, Y. Zhou, A. M. Korsunsky, H. Bhaskaran, M. Terrones, J. H. Warner, *ACS Appl. Mater. Interfaces* **2017**, *9*, 15005.
- [27] Y. C. Lin, S. S. Li, H. P. Komsa, L. J. Chang, A. V. Krasheninnikov, G. K. Eda, K. Suenaga, *Adv. Funct. Mater.* **2018**, *28*, 1704210.
- [28] Z. L. Hu, J. Avila, X. Y. Wang, J. F. Leong, Q. Zhang, Y. P. Liu, M. C. Asensio, J. P. Lu, A. Carvalho, C. H. Sow, A. H. C. Neto, *Nano Lett.* **2019**, *19*, 4641.
- [29] N. Saigal, S. Ghosh, *Appl. Phys. Lett.* **2016**, *109*, 122105.
- [30] X. X. Zhang, Y. You, S. Y. Zhao, T. F. Heinz, *Phys. Rev. Lett.* **2015**, *115*, 257403.
- [31] A. Arora, K. Nogajewski, M. Molas, M. Koperski, M. Potemski, *Nanoscale* **2015**, *7*, 20769.
- [32] A. Arora, M. Koperski, K. Nogajewski, J. Marcus, C. Faugeras, M. Potemski, *Nanoscale* **2015**, *7*, 10421.
- [33] K. P. O'donnell, X. Chen, *Appl. Phys. Lett.* **1991**, *58*, 2924.
- [34] Y. P. Varshni, *Physica* **1967**, *34*, 149.
- [35] M. A. Khan, M. Erementchouk, J. Hendrickson, M. N. Leuenberger, *Phys. Rev. B* **2017**, *95*, 245435.
- [36] P. E. Blochl, *Phys. Rev. B* **1994**, *50*, 17953.
- [37] G. Kresse, J. Furthmuller, *Phys. Rev. B* **1996**, *54*, 11169.
- [38] J. Klimeš, D. R. Bowler, A. Michaelides, *Phys. Rev. B* **2011**, *83*, 195131.
- [39] H. J. Monkhorst, J. D. Pack, *Phys. Rev. B* **1976**, *13*, 5188.